

## Research Article

# Dielectric Properties and 3D-Printing Feasibility of UV-Curable Resin/Micron Ceramic Filler Composites

Yijia Fu , Wendong Li , Man Xu , Chao Wang , Liyuan Zhang , and Guanjun Zhang 

State Key Laboratory of Electrical Insulation and Power Equipment, Xi'an Jiaotong University, 710049 Xi'an, China

Correspondence should be addressed to Man Xu; xumman@mail.xjtu.edu.cn

Received 14 August 2021; Revised 3 February 2022; Accepted 4 February 2022; Published 27 February 2022

Academic Editor: Sébastien Déon

Copyright © 2022 Yijia Fu et al. This is an open access article distributed under the Creative Commons Attribution License, which permits unrestricted use, distribution, and reproduction in any medium, provided the original work is properly cited.

To prepare high-permittivity composite materials for dielectrically functional gradient materials (d-FGMs) by the stereolithographic 3D-printing technique, three ceramic powders (i.e., alumina, barium titanate, and strontium titanate) are selected as functional fillers for a UV-curable resin matrix. The viscosity and UV curing depth of the uncured slurry are tested for feasibility of 3D printing. Comprehensive electrical properties, including volume resistivity, permittivity, dielectric loss, and breakdown strength of the cured composites are measured. The effects of the filler types, morphologies, particle sizes, and volume fractions on the UV curing characteristics of the slurry and dielectric properties of cured composites are systematically analyzed. The experimental results show that spherical fillers with large particle sizes, smooth surfaces, and high permittivity are conducive for reducing the slurry viscosity, increasing curing depth and adjusting the composite's permittivity over a wide range. We believe that the proposed strategy for material system establishment can improve the 3D printability of high-permittivity composites and promote other applications of the d-FGMs by the stereolithography technique.

## 1. Introduction

High-voltage power equipment requires strong insulation systems [1]. However, their breakdown caused by distorted electric fields is a widespread engineering problem. To ensure a uniform electric field distribution and enhance the electrical performance of the insulation system, conventional methods include adjusting the electrode-insulation structure (“shape control”), such as adding a grading ring or a shielding cover [2–4]. This method often results in limited optimization and a complicated insulation structure that not only increases the difficulty of installation, operation, and maintenance but also does not meet the requirements of compact design [5, 6].

Some researchers have considered solving this problem from the perspective of insulator bulk and proposed the concept of functional gradient materials (FGMs). Electric fields could be regulated by constructing nonuniform distributions of the dielectric parameters inside insulators [7, 8]. By controlling the permittivity or electrical conductivity distribution of the composite, the electric field can be actively

controlled to alleviate distortions and formation of local regions; such insulation structures could be summarized as dielectrically functional gradient materials (d-FGMs) [9, 10]. Among them, the permittivity gradient materials ( $\epsilon$ -FGMs) are suited to uniform electric field distributions under AC/impulse voltage and have large potential for simplifying the insulation structure. The existing methods of manufacturing  $\epsilon$ -FGM include lamination and centrifugation. However, poor controllability and flexibility in the design and fabrication stages restrict their industrial applications. In recent years, 3D-printing technology, also known as additive manufacturing, has provided a new strategy for fabrication of FGMs [11]. By controlling the permittivities of the materials “layerwise”,  $\epsilon$ -FGMs with nonuniform spatial distributions can be obtained. Commonly used 3D-printing technologies include Fused Deposition Modeling (FDM), Selective Laser Sintering (SLS), and Stereo Lithography Apparatus (SLA). Among them, the SLA technology has advantages in molding accuracy and internal defect control, which is more suitable for high-voltage insulation systems.

SLA technology is using a UV laser to scan the UV-curable resin to cure and build it layer by layer based on a preset shape. A typical SLA printer is shown in Figure 1. The laser irradiates from the bottom of the transparent resin tank according to the set shape to cause the cross-linking of the resin. After the single layer is cured and formed, the lifting platform moves up to a certain height, which is the single-layer printing thickness. Then, the laser scanning initiates the curing of a new layer of UV resin, and each of the resin layers is connected by chemical bonds until the printing is completed.

One of the key factors in printing  $\epsilon$ -FGM using SLA is that the permittivity of the UV-cured composite should be adjustable over a wide range. To achieve this, a UV-curable resin with high permittivity as an inorganic filler is the conventional method. However, high loading ratios are needed to increase the upper limit of the composite permittivity, resulting in high viscosity and poor single-layer printing thickness. It is not conducive to the smooth leveling and curing of printed materials. In this case, poor printability increases the printing failure rate significantly [12]. However, the influences of filler characteristics on the dielectric properties and related printability have seldom been reported in literature.

In order to improve the permittivity of the composites, two kinds of ceramic fillers (barium titanate and strontium titanate) with different particle sizes ( $\sim 40 \mu\text{m}$  and  $\sim 4 \mu\text{m}$ ) and high intrinsic permittivities (3000 and 300) are adopted. For the purpose of maintaining the stability of the viscosity of the slurry along the gradient direction to reduce the difficulty of printing and avoiding a major impact on its dielectric properties, we would like to build a double-filler system, so choose alumina with different sizes ( $\sim 40 \mu\text{m}$  and  $\sim 4 \mu\text{m}$ ) and low intrinsic permittivity ( $\epsilon_r = 10$ ) as another filler, which has good light transmittance, high thermal conductivity, low loss, etc. We investigate the influence of the filler type, morphology, particle size, and filling content on the dielectric properties of composites and related properties (viscosity and UV curing depth) in order to provide a good selection for the preparation of  $\epsilon$ -FGM insulators by SLA technology. We have obtained composites with high permittivities by adding  $\text{BaTiO}_3$  powders and achieved surprising results by spheroidizing  $\text{Al}_2\text{O}_3$  powder at high temperature. The spherical fillers have good dispersibility in the composites and significantly reduce their viscosities. Meanwhile, the curing depths of the composites can be improved by increasing the UV exposure energy and choosing fillers with large particle sizes. We intend that this work would be a suitable reference for the preparation of  $\epsilon$ -FGM insulators by SLA.

## 2. Experimental

**2.1. Materials.** UV resin (High Temp; HT) with excellent mechanical properties and heat resistance was purchased from Formlabs Inc. (Somerville, Massachusetts, USA). Because the composite materials evaluated in this study are applied to insulation, we compared the dielectric properties

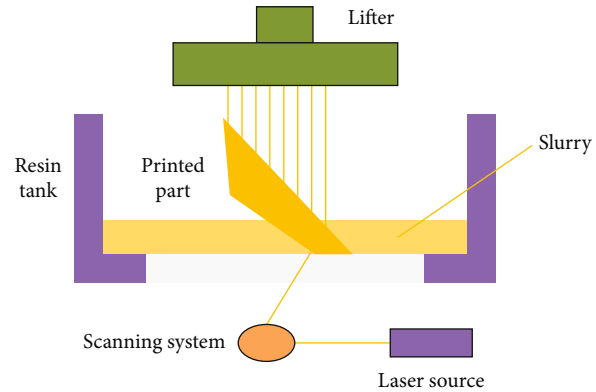


FIGURE 1: Schematic diagram of SLA technology.

TABLE 1: Dielectric properties of the UV-curable resin HT and epoxy resin E51.

Properties	HT	E51
Relative permittivity	3.4	3.2
Dielectric loss	$7.5 \times 10^{-3}$	$3.6 \times 10^{-3}$
Volume resistivity ( $\Omega\text{m}$ )	$2.6 \times 10^{14}$	$6.0 \times 10^{14}$
Breakdown strength (kV/mm)	36.2	36.7

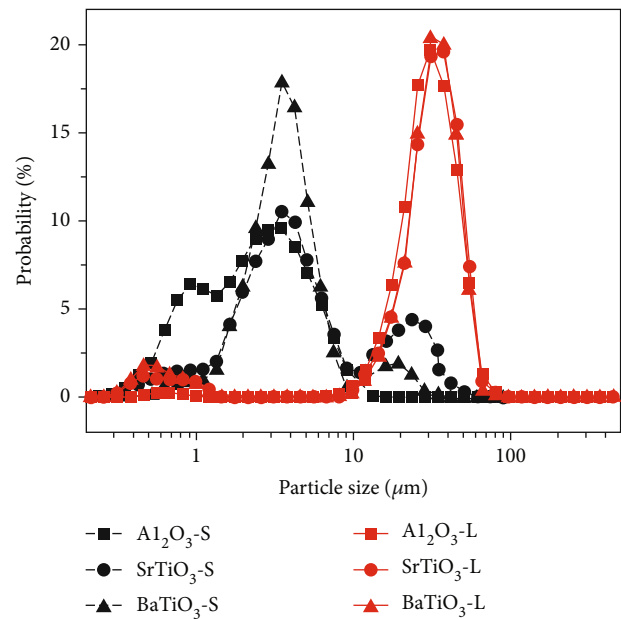


FIGURE 2: Particle size distributions of the various fillers.

of the UV resin with epoxy resin E51, which is commonly used for insulation. The samples (100 mm diameter, 1 mm thickness, disc) were tested, the epoxy resin sample was mixed with bisphenol A epoxy resins, anhydride curing agent (MEHHPA), and accelerator (DMP-30) in a mass ratio of 100:90:0.4. The slurry was poured into the mold after vacuum degassing and then heat curing at 120°C for 6 h. The UV-curable resin sample was 3D printed with an

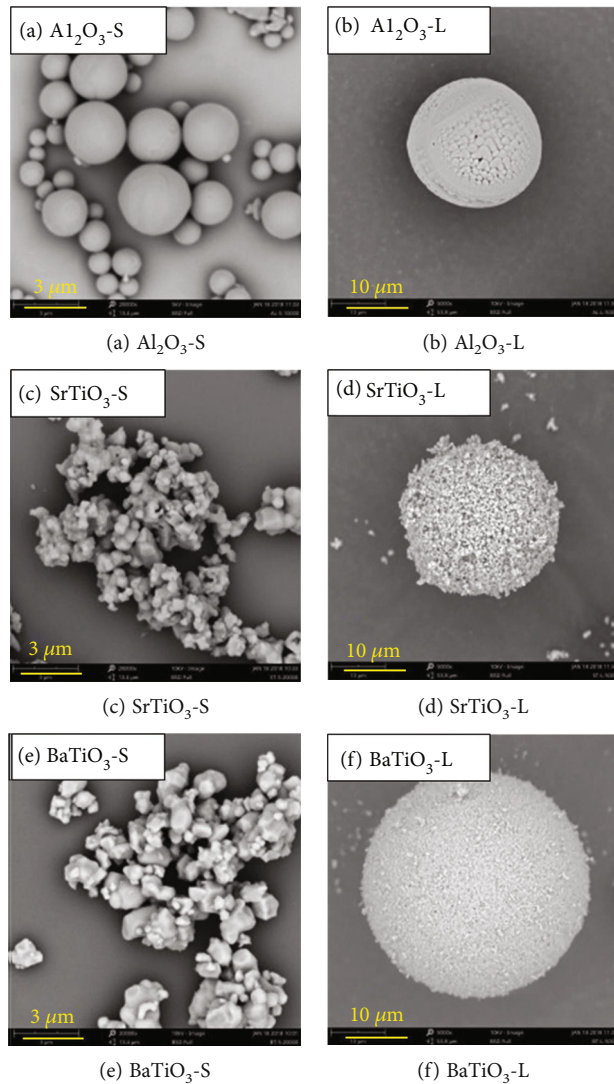


FIGURE 3: Microscopic morphologies of the filler particles.

SLA printer (Formlabs Form2) and cured at 60°C for 2 h after UV exposure. The specific test method is as follows:

- (1) The relative permittivity and dielectric loss are tested by using Tettex 2821 high-voltage Xilin bridge, room temperature atmosphere, and externally applied 0.5 kV power frequency voltage. Test standard reference GBT 1409-2006
- (2) The volume resistivity is tested by Keithley 6517B picoammeter and 8009 fixture, room temperature atmosphere, and 0.5 kV DC voltage
- (3) The experimental standard of the breakdown strength follows IEC 60243-1 :1998, immersing the sample and ball-ball electrode in transformer oil at room temperature, the boost rate of Power frequency AC is 1 kV/s

From Table 1, the results indicate that these two resins have similar dielectric properties. Therefore, the UV resin can be used as a replacement for E51 in electrical insulation.

The three ceramic powders  $\text{Al}_2\text{O}_3$  (Shanghai Baitu Advanced Materials Technology Co., Ltd., Shanghai, China),  $\text{BaTiO}_3$ , and  $\text{SrTiO}_3$  (Shanghai Dianyang Industrial Co., Ltd., Shanghai, China) were adopted as the fillers. These fillers have large (L) and small (S) particle sizes, and the particle size distribution of the fillers was tested using a laser particle size analyzer (OMEC LS-POP (6), Zhuhai, China). Figure 2 depicts that the  $D_{50}$  ( $\sim 40 \mu\text{m}$ ) of the large-sized particle fillers is about ten times that ( $\sim 4 \mu\text{m}$ ) of the small-sized particle fillers and that both the large and small sized fillers have lower size dispersion.

The filler particles were observed by scanning electron microscopy (SEM, Phenom Pro, Eindhoven, Netherlands). One gram of a filler was added to about 20 mL of ethanol absolute, and 1 mL of this suspension was placed on a polished silicon wafer after stirring for testing after drying. The fillers were evaluated after the gold spraying treatment.

Figure 3 illustrates the SEM image of the filler particles, showing the three kinds of large-sized particle fillers which have regular spherical morphology.  $\text{BaTiO}_3$ -L and  $\text{SrTiO}_3$ -

L had similar morphologies and were composed of small particles that were bonded loosely. Although the particles inside the  $\text{Al}_2\text{O}_3$ -L are bonded tightly, there are still pores. For small-sized particle fillers,  $\text{Al}_2\text{O}_3$ -S has a regular spherical shape, while the shapes of  $\text{BaTiO}_3$ -S and  $\text{SrTiO}_3$ -S are not regular.

The differences in the microscopic morphologies of the filler particles are related to their preparation processes. The  $\text{Al}_2\text{O}_3$ -S and  $\text{Al}_2\text{O}_3$ -L undergo flame spheroidization, such that a spherical morphology and dense structure of the filler particles are obtained after experimenting with a series of endothermic, melting, and cooling transition processes in the high-temperature flame stream [13]. While the  $\text{SrTiO}_3$ -S and  $\text{BaTiO}_3$ -S were prepared by solid-phase calcination where it is difficult to control the microscopic morphologies of the fillers,  $\text{SrTiO}_3$ -L and  $\text{BaTiO}_3$ -L were prepared by the spray drying method. Although the filler particles had spherical shapes, their structures are relatively loose because the insides of the particles were not heat treated at high temperatures, and the grains were only bonded to each other by van der Waals forces [14].

**2.2. Specimen Preparation.** The  $\text{Al}_2\text{O}_3$ ,  $\text{BaTiO}_3$ , and  $\text{SrTiO}_3$  fillers with large and small particle sizes were used to prepare the UV-cured composite material samples with different volume fractions (5, 10, 15, and 20 vol%). UV resin was used directly after unpacking, and the fillers were predried in a vacuum for 8 h at 100°C. A certain amount of the fillers was added into UV-curable resin and then mixed by a planetary centrifugal mixer (ZD-TJ500A, Shenzhen Zhidi Technology Co., Ltd., China) for 30 min maximum with 100 rpm rotation and revolution speeds. During the stirring process, vacuum ambient (<100 Pa) and elevated temperature (50°C) were adopted to remove the increase fluidity and internal air bubbles. Finally, six UV composite slurries were obtained. The label of the slurries is shown in Table 2.

As shown in Figure 4(a), to obtain samples with regular shapes and uniform thickness, a light curing scheme with closed molds for shape constraints was proposed. The specific steps are as follows: (1) The mold is made of a 0.5 mm thick silicone sheet placed on a quartz glass bottom plate (the bottom surface is close to the polyester release film; PET release film); (2) UV composite slurry was injected into the mold, and the quartz cover plate (with the PET release film on the lower layer) was pressed onto the mold plate; (3) the mold was then placed in the UV curing box and cured for 2 h under 405 nm UV exposure (20 mW/cm<sup>2</sup>) at 60°C. Figures 4(b) and 4(c) show that the obtained samples have regular shapes, uniform thickness, smooth surfaces, and no warpage.

### 2.3. Testing and Characterization

**2.3.1. Microscopic Morphologies.** The cross-sectional fracture surface of the cured composites was observed by the scanning electron microscopy after low-temperature cracking in liquid N<sub>2</sub> and magnetron sputtering of nm-thickness surface gold layer. The method is the same as the observation method of the fillers.

TABLE 2: The label of the slurries.

Sample	Vol (%)	Label
$\text{Al}_2\text{O}_3$ -L	5	HT/AL-L-5
	10	HT/AL-L-10
	15	HT/AL-L-15
	20	HT/AL-L-20
$\text{SrTiO}_3$ -L	5	HT/ST-L-5
	10	HT/ST-L-10
	15	HT/ST-L-15
	20	HT/ST-L-20
$\text{BaTiO}_3$ -L	5	HT/BT-L-5
	10	HT/BT-L-10
	15	HT/BT-L-15
	20	HT/BT-L-20
$\text{Al}_2\text{O}_3$ -S	5	HT/AL-S-5
	10	HT/AL-S-10
	15	HT/AL-S-15
	20	HT/AL-S-20
$\text{SrTiO}_3$ -S	5	HT/ST-S-5
	10	HT/ST-S-10
	15	HT/ST-S-15
	20	HT/ST-S-20
$\text{BaTiO}_3$ -S	5	HT/BT-S-5
	10	HT/BT-S-10
	15	HT/BT-S-15
	20	HT/BT-S-20

**2.3.2. Dielectric Properties.** The relative permittivity ( $\epsilon_r$ ), dielectric loss ( $\tan\delta$ ), volume resistivity ( $\rho_v$ ), and breakdown strength ( $E_b$ ) were tested using the samples (85 mm diameter, 0.5 mm thickness, disc). The test methods are consistent with the UV-curable resin HT and epoxy resin E51. For the breakdown strength, each sample was assessed 15 times repeatedly, and the Weibull distribution was used for fitting.

**2.3.3. 3D-Printing-Related Performance.** The dynamic viscosity of the uncured slurry was characterized by a rotational viscometer (NDJ-79A, Shanghai Changji Instrument Co., Ltd., China) at the shear rate of about 40 s<sup>-1</sup>, and the temperature of the water bath was increased from 30 to 70°C, with the viscosity being tested every 10°C. To investigate the UV curing depth, the resin was poured into a polytetrafluoroethylene (PTFE) vessel (5 mm depth) and irradiated with UV light (5 mW/cm<sup>2</sup>) [15]. The cured sheet was cleaned with isopropanol, and its depth was measured with a feeler after removing the uncured slurry (0.001 mm precision).

## 3. Results and Discussion

**3.1. Microscopic Morphologies of the Composite Material Sections.** The brittle sections of the composite materials with small- and large-sized particle fillers are shown in Figures 5 and 6, respectively. Two main phenomena can be observed from these images: (1) Agglomeration—as shown in

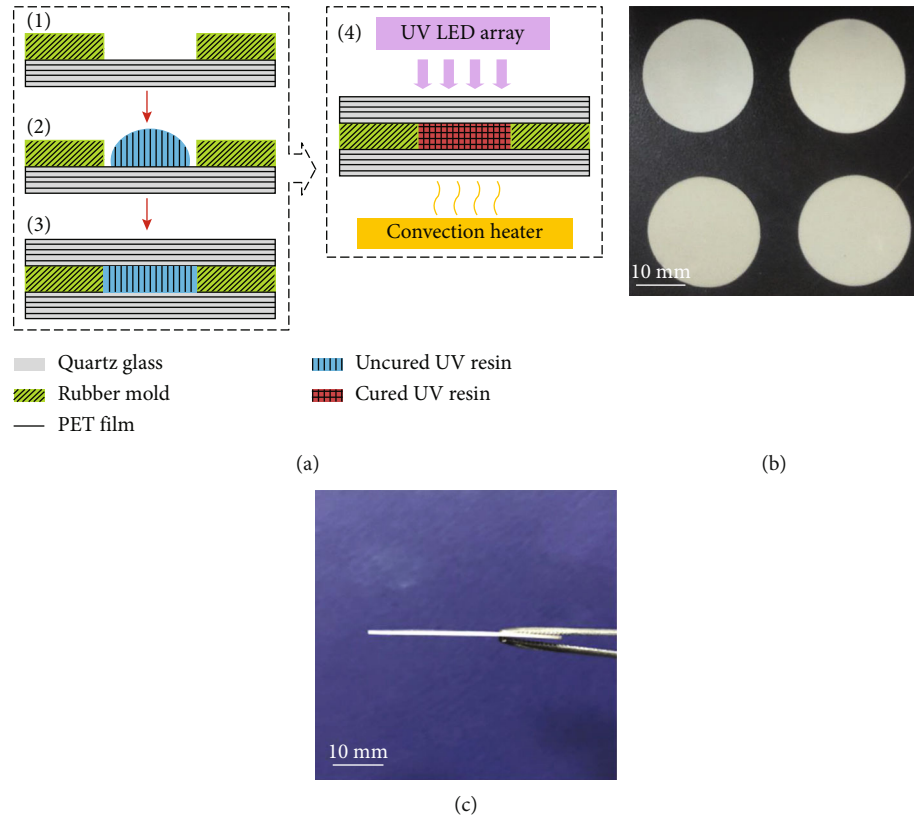


FIGURE 4: (a) Pouring and curing, (b) top view of the samples, and (c) lateral view of samples.

Figure 5, agglomeration occurs in the HT/ST-S and HT/BT-S composites because of the higher surface energies owing to the small particle sizes. The higher the filler content, the greater is the agglomeration. However, spherical fillers with both large and small particle sizes always maintain good dispersibility and no obvious agglomerations in the resin. (2) Settlement—for composite materials with small-sized particle fillers (Figure 5), settlement in the UV resin is relatively weak owing to the low gravity. For composite materials with large-sized particle fillers (Figure 6), the intermolecular forces are smaller when the filler content is low, and stratification is obvious because of their own gravity. While the filler content is high, the settlement disappears because of enhancements of the intermolecular forces and viscosities.

**3.2. Dielectric Properties.** One of the key factors in printing  $\epsilon$ -FGMs through SLA is that the permittivities of the UV-cured composites should be adjustable over a wide range. Thus, we first consider the influences of the filler types, particle sizes, and volume fractions on the dielectric properties (volume resistivity, relative permittivity, dielectric loss, and breakdown strength).

The volume resistivity of a composite depends on the number and mobilities of the carriers that are mainly attributable to the impurity ions contained in the fillers. Figure 7(a) depicts that  $\rho_v$  decreases as the volume fraction increases, except for the HT/AL-S composite; this phenomenon is related to enhancement of the conduction process in the composites, which is due to the increase in carrier

concentration with the introduction of fillers. Furthermore, as the volume fraction increases, the contact between the particles will increase the possibility of carrier migration. For instance, Figure 5 depicts that there is agglomeration in both the HT/ST-S-5 and HT/BT-S-5 composites, causing overlapping of the interface area and possibly increasing the mobilities of the carriers.

In the HT/AL-S composites, as the volume fraction increases,  $\rho_v$  rises slightly; it can be considered that the specific surface area of the  $\text{Al}_2\text{O}_3$ -S fillers increases sharply compared to that of the  $\text{Al}_2\text{O}_3$ -L fillers with increase in volume fraction, and the surface atoms account for a large proportion of the total number of atoms in the particles. Because there are no adjacent atoms around the surface, the surface atoms have many dangling bonds which result in high chemical activity. Fillers therefore have strong interactions with the UV resin matrix to generate more interfaces because of the high chemical activity. However, the structure of the fillers is denser, and the interface areas act as traps to capture carriers. The carriers frequently sink during the migration, which reduces their mobility and increases  $\rho_v$ . Moreover, the dispersion of particles in the UV resin is good without obvious agglomeration.

Figure 7(c) shows the trend of the relative permittivity  $\epsilon_r$  of the composite with increasing volume fraction of fillers. The relative permittivity of the composite increases with addition of the volume fraction  $V_f$ . Among the three fillers,  $\text{BaTiO}_3$  improves the permittivity of the composite materials the most, when  $V_f$  reaches 20%,  $\epsilon_r$  increases to 7.6 in the HT/

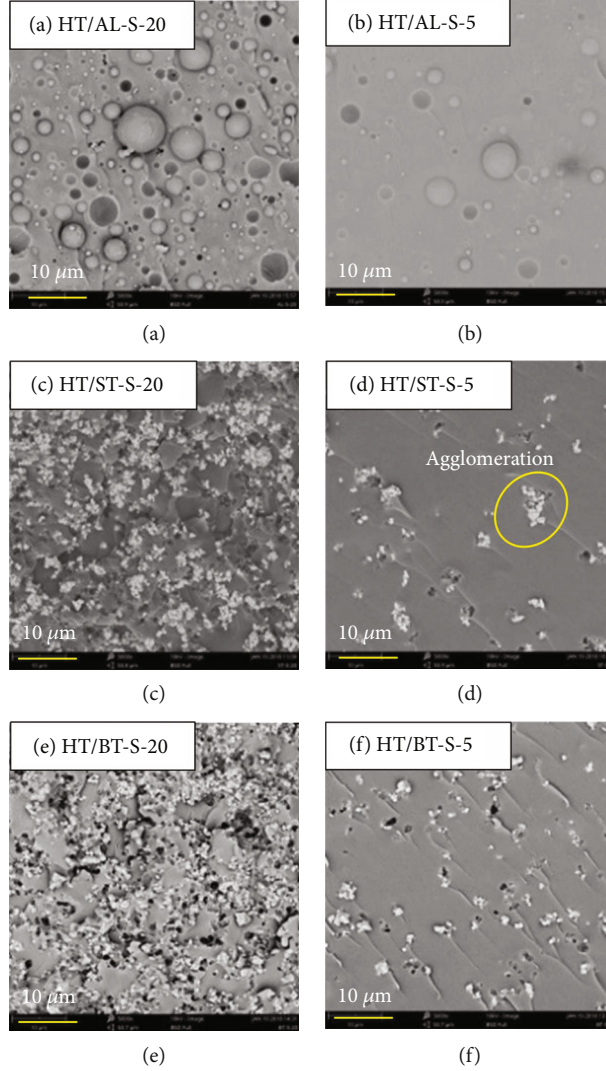


FIGURE 5: Cross-sectional images of the composites with small-sized filler particles.

BT-S composites. However, the addition of  $\text{Al}_2\text{O}_3$  has little effect on the permittivity of the HT/AL composites. Meanwhile, the improvement in the relative permittivities of the composites with small-sized filler particles is better than that with large-sized filler particles.

For the above phenomenon, we believe that the intrinsic permittivity for  $\text{BaTiO}_3$  ( $\epsilon_r = 3000$ ) is higher than that of  $\text{SrTiO}_3$  ( $\epsilon_r = 300$ ) and much larger than that of  $\text{Al}_2\text{O}_3$  ( $\epsilon_r = 10$ ). The higher the intrinsic permittivity of the filler, the more obvious is the increase in the relative permittivity of the composite for the same volume fraction. In the micro-composites, the relative permittivity depends not only on the intrinsic permittivity of the filler and UV resin matrix but also on the particle sizes of the fillers, volume fraction of the fillers, and interface polarization between the fillers and UV resin matrix.

We use the Maxwell-Garnett model to predict the relative permittivity of composites, which is applicable to lower filler loading [16]. According to the Maxwell-Garnett equation, the relative permittivity of the composites can be characterized as

$$\epsilon = \epsilon_m \left[ 1 + \frac{3V_f(\epsilon_f - \epsilon_m)}{(1 - V_f)(\epsilon_f - \epsilon_m) + 3\epsilon_m} \right], \quad (1)$$

where  $\epsilon$  is the relative permittivity of the composite,  $\epsilon_m$  is the relative permittivity of the UV resin matrix,  $\epsilon_f$  is the intrinsic permittivity of the filler, and  $V_f$  is the volume fraction of the filler.

The fitting results are shown in Figure 7(b). It is seen that the results are about 14% lower than the actual relative permittivity value, which may indicate that the interface polarization increases the relative permittivity. Because the small-sized particle fillers have larger specific surface areas, which enhance the surface energies of the particles and their surface activities, the surface atoms are extremely unstable so that the composites with small-sized filler particles have stronger interface polarizations. Therefore, the increase in the relative permittivity of the composite with small-sized filler particles is slightly better than that with large-sized filler particles.

Figure 7(d) depicts that the  $\tan\delta$  of the composites increases with increase in the volume fractions of the fillers,

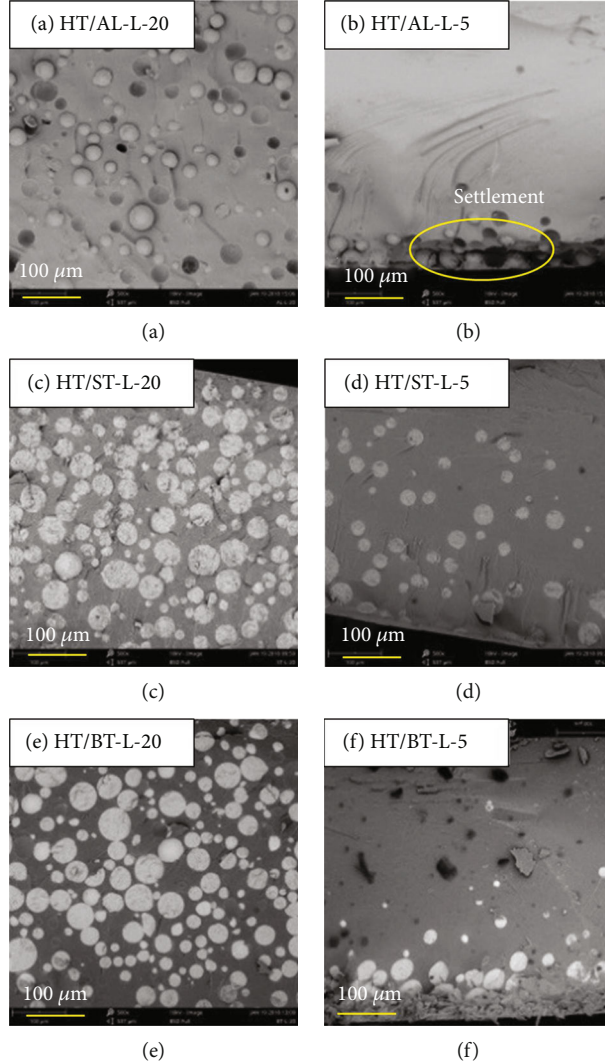


FIGURE 6: Cross-sectional images of the composites with large-sized filler particles.

except for the HT/AL-S composites. The  $\tan\delta$  depends on the conductivity and polarization losses of the composites. The conductivity of the composites depends on the number and mobility of carriers. The introduction of these two fillers enhances the carrier concentrations in the composites, and the  $\text{BaTiO}_3$  and  $\text{SrTiO}_3$  fillers have relatively high  $\tan\delta$  and low  $\rho_v$  [17], thereby increasing the overall material loss and electrical conduction process. In addition,  $\text{BaTiO}_3$  and  $\text{SrTiO}_3$  are ferroelectrics, and the domain dipole moments generated by spontaneous polarization result in orientation polarization under the action of an electric field, which causes polarization loss. For the HT/AL-L composites, there are mainly electronic and ionic displacement polarizations in the electric field. Although the loss caused by these two polarizations is small, the  $\tan\delta$  still exhibits an increasing trend owing to enhancement of the concentrations and mobilities of the carriers. Finally, the interface polarization caused by the impurities and interface defects in the composites introduced by the inorganic fillers also improves the dielectric loss [18] in the above composite systems.

For the HT/AL-S composites, the dielectric losses decrease slightly as the volume fraction increases. On the one hand, because the  $\text{Al}_2\text{O}_3$ -S fillers mainly exhibit electronic and ionic displacement polarizations under the action of an electric field, the polarization loss is low [19]. On the other hand, the carriers frequently sink during migration in the HT/AL-S composites, resulting in reduced carrier mobility; further, the entanglement of the polymer chains hinders migration of the carriers. These causes decrease the dielectric loss  $\tan\delta$  in the HT/AL-S composites.

The breakdown strength  $E_b$  of the composite is processed using a Weibull distribution [20, 21], and the results are shown in Figure 8. Meanwhile, the scale parameter  $\beta$  and shape parameter  $\gamma$  can be obtained; the scale parameter  $\beta$  represents the breakdown strength with a failure probability of 63.2%, and the shape parameter  $\gamma$  reflects the dispersion of the breakdown strength. The larger the value of  $\gamma$ , the smaller is the dispersion.

Figure 9(a) illustrates the trend of the scale parameter  $\beta$  with change in the volume fraction of the filler  $V_f$ . It is seen

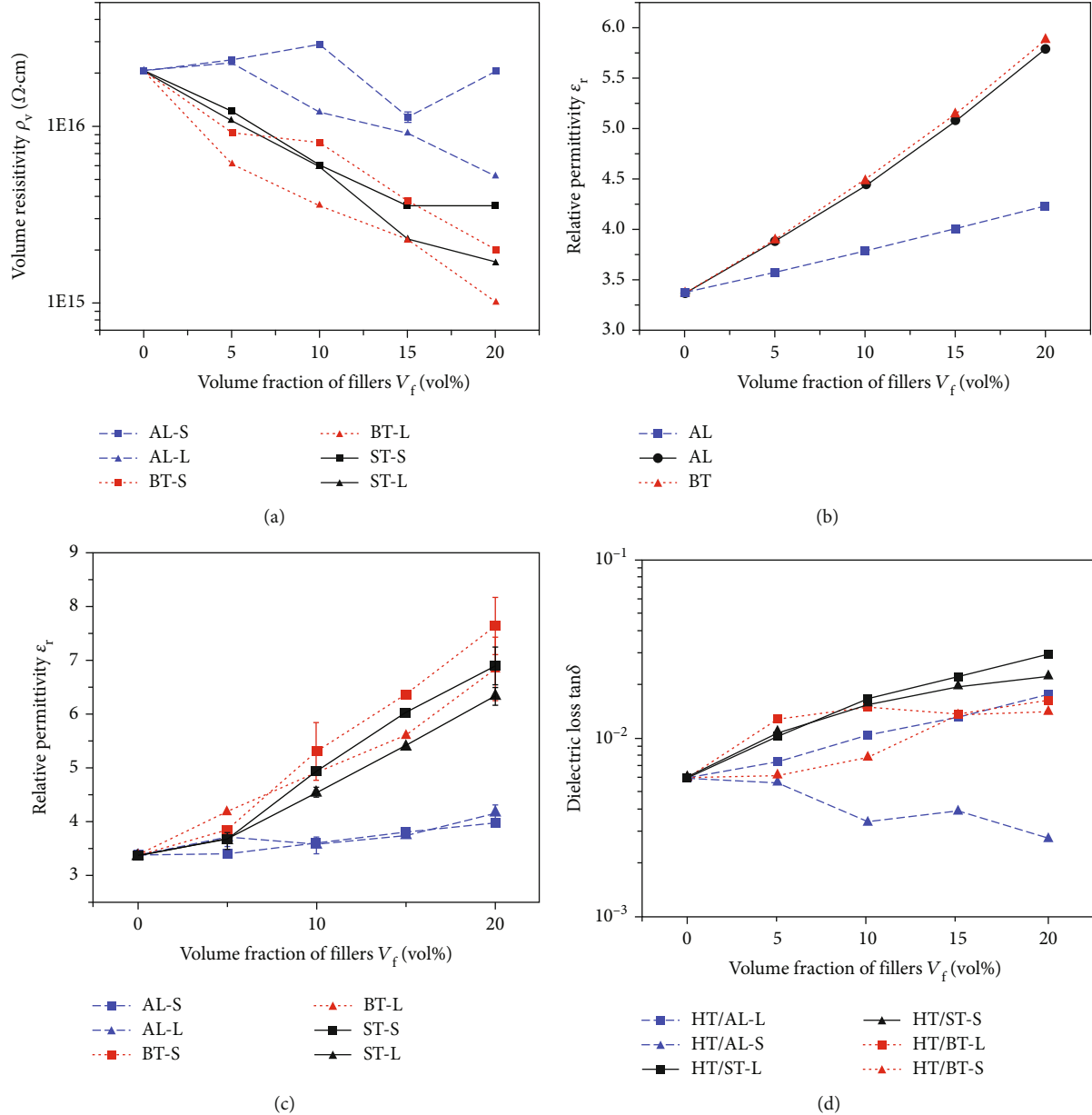


FIGURE 7: (a) Volume resistivities of the composites, (b) permittivities of the composites fitted with the Maxwell–Garnett formula, (c) permittivities of the composites, and (d) dielectric losses of the composites.

that  $\beta$  of the HT/BT and HT/ST composites decreases significantly with increase in  $V_f$ , whereas the  $\beta$  of the HT-AL composites does not change much. There is no obvious correlation between  $\beta$  and the particle sizes of the fillers. For the HT/BT and HT/ST composites, the differences between the relative permittivities of the fillers and UV resin matrix are larger, and strong electric field distortions exist in the filler-resin interface region, which decreases the breakdown strength. For the HT/AL composites, the difference between the relative permittivity of the fillers and UV resin matrix is small, and frequent sinking of the carriers in the composites reduces their mobility and kinetic energy such that the breakdown strength changes minimally.

As shown in Figure 9(b), the shape parameter  $\gamma$  of the other composites decreases insignificantly compared with that of the UV resin except for composites filled with 10 vol%  $\text{BaTiO}_3$ -S. The above phenomenon means that the dispersion of the breakdown strength remains stable. For composites filled with 10 vol%  $\text{BaTiO}_3$ -S fillers, the decrease in the shape parameter  $\gamma$  may be related to agglomeration of the fillers. Agglomeration causes local weak points in the composites, which reduce their uniformity and increase the dispersion of the breakdown strength.

In the final analysis, the introduction of inorganic fillers, especially  $\text{BaTiO}_3$  with high permittivities, can help improve the adjustable range of relative permittivity of the composites and enhance the electric field homogenization effects

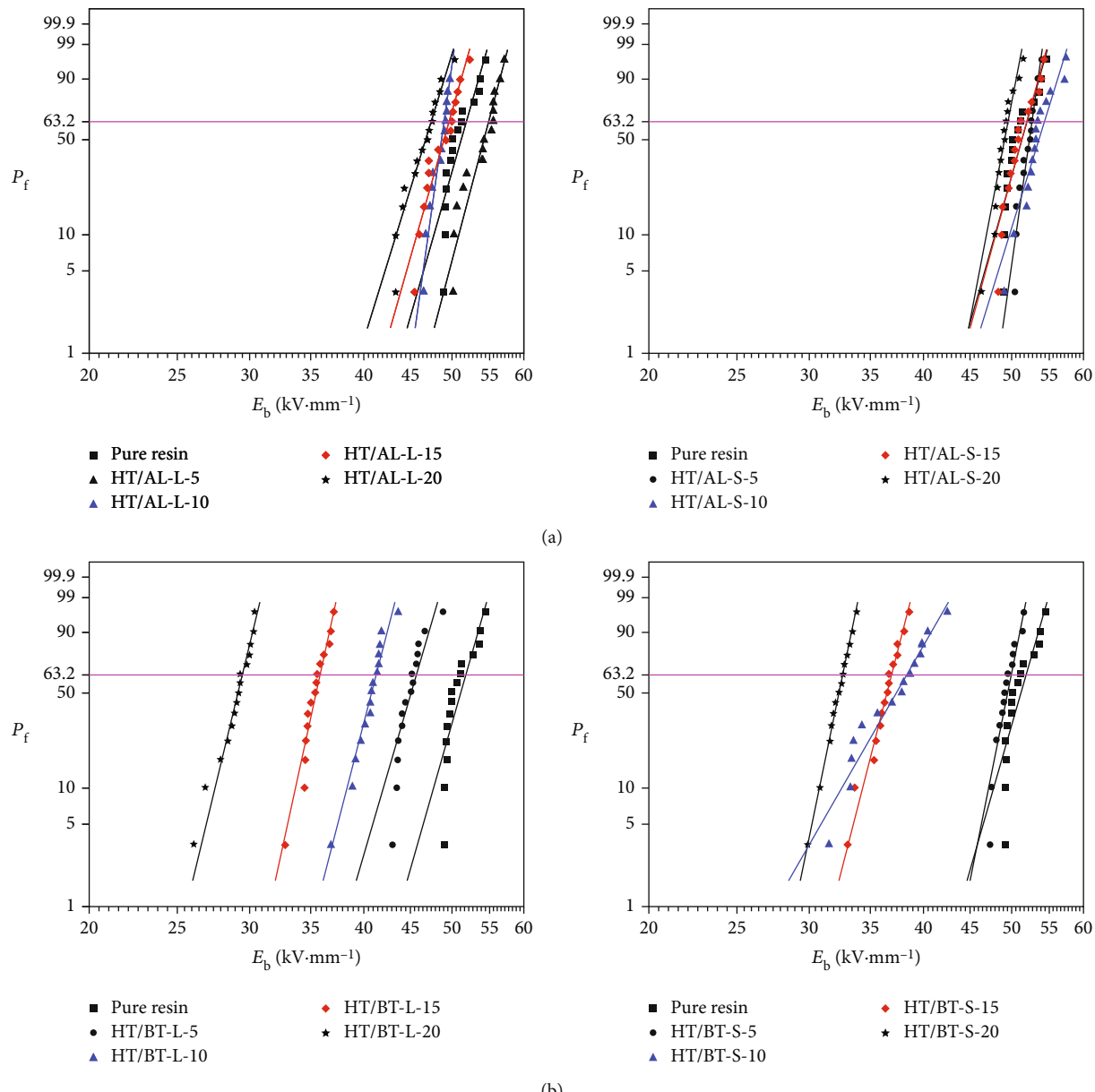


FIGURE 8: Continued.

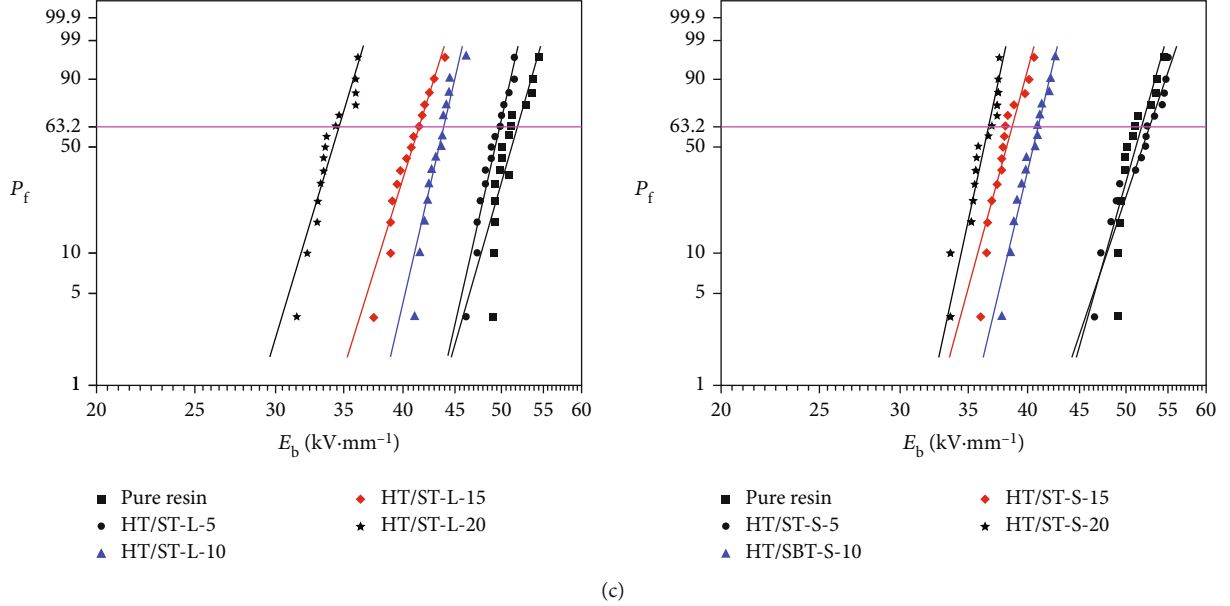


FIGURE 8: Weibull distributions of the breakdown strengths of (a) HT/AL-L and HT/AL-S, (b) HT/BT-L and HT/BT-S, and (c) HT/ST-L and HT/ST-S.

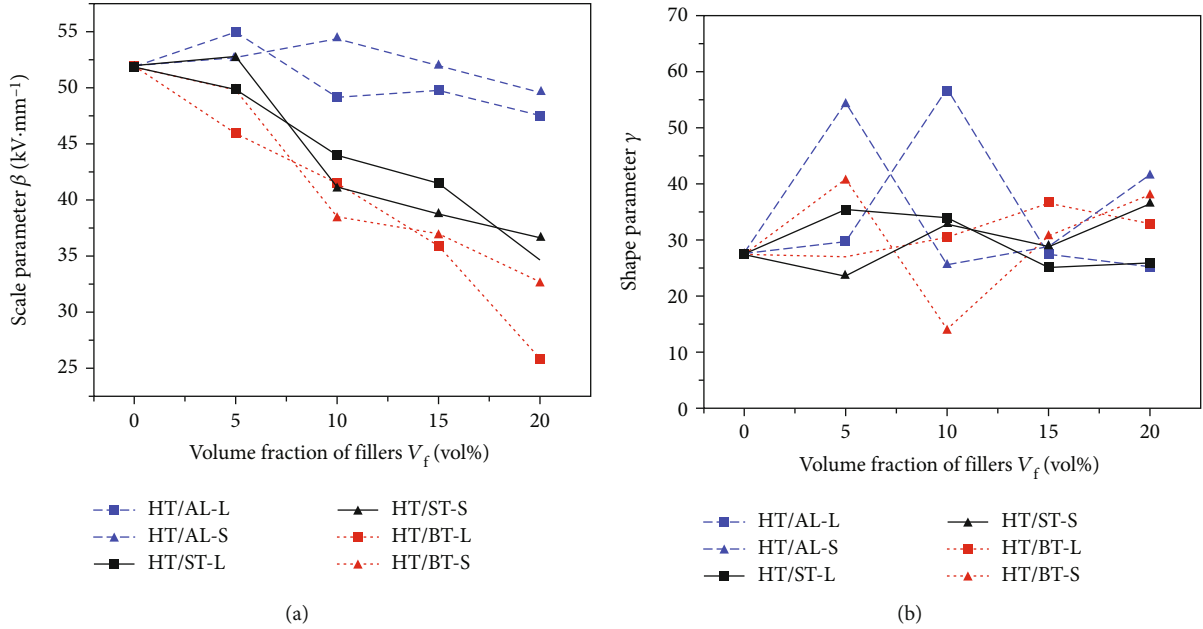


FIGURE 9: (a) Scale parameter  $\beta$  of the breakdown strength, and (b) shape parameter  $\gamma$  of the breakdown strength.

of the  $\varepsilon$ -FGMs [22], which is beneficial for flashover voltage along the insulator. Meanwhile, the addition of  $\text{Al}_2\text{O}_3$  has little influence on the dielectric properties of the composites, which also verifies our conjecture.

**3.3. 3D-Printing Performances.** To obtain  $\varepsilon$ -FGMs by SLA, the viscosities of the uncured slurries and UV curing depths of the composites are considered. The maximum viscosity of the UV resin available for SLA is 3000 mPa·s [12]. Any viscosity exceeding 3000 mPa·s will affect the self-leveling pro-

cess of the slurry during printing, thus reducing the printing precision and success rate. Figure 10(a) shows the relationship between the viscosity  $\eta$  of the uncured slurries and volume fractions of the fillers  $V_f$  at 30°C. It is seen that  $\eta$  of uncured slurry is nonlinearly dependent to solid loading. In general, the  $\eta$  of the uncured slurries increase with increase in  $V_f$ . Aside from the similar behaviors, quantitative difference can be observed between different slurries. When  $V_f$  is the same,  $\eta$  of the uncured HT/BT and uncured HT/ST slurries are similar and are much higher than that of

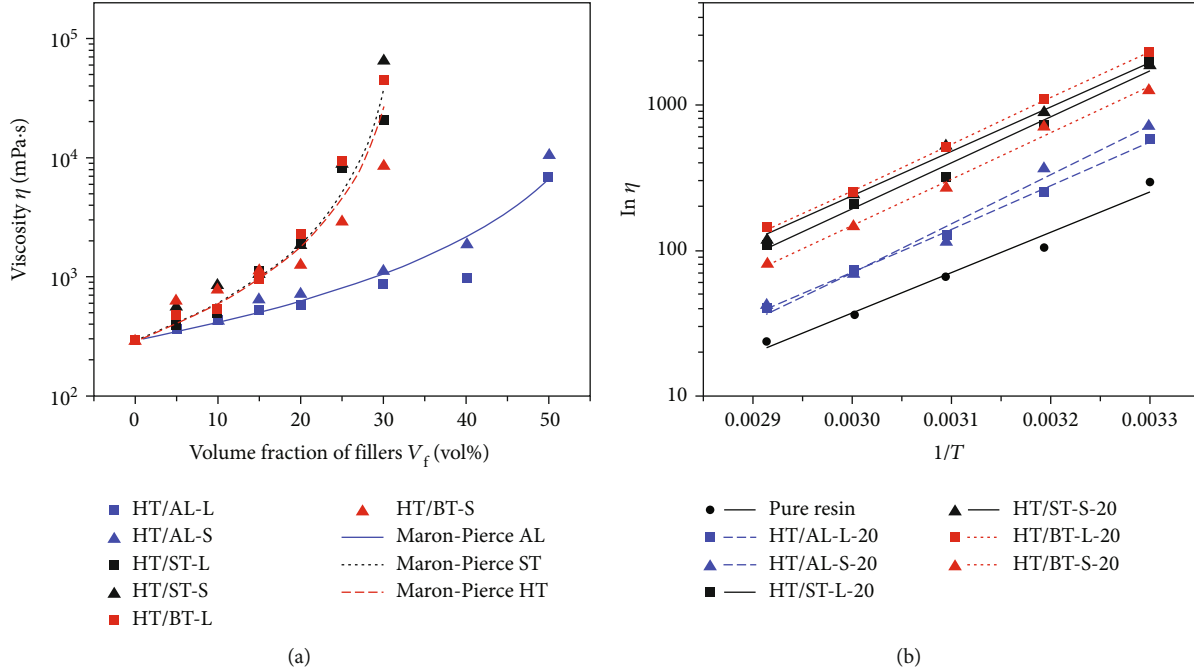


FIGURE 10: (a) Viscosities of the uncured slurries at 30°C, and (b) viscosity–temperature relationship of the pure resin and six uncured slurries.

the uncured HT/AL slurry. For example, when  $V_f$  is 20 vol%, the viscosity  $\eta$  of the uncured HT/BT-L and HT/ST-L slurries are 2280 mPa·s and 1950 mPa·s, respectively, which are much higher than that of the uncured HT/AL-L slurry (581 mPa·s). The uncured slurries will lose fluidity and are difficult to use in SLA when the  $V_f$  of BaTiO<sub>3</sub> and SrTiO<sub>3</sub> exceed 30 vol%. However, the uncured slurries filled with Al<sub>2</sub>O<sub>3</sub> still have a certain fluidity when  $V_f$  reaches 50 vol%. It is worth noting that the particle sizes of the fillers have little effects on the viscosities of the uncured slurries, which is consistent with published work [23]. According to the 3D-printing requirement that the viscosity be less than 3000 mPa·s, the uncured HT/AL slurry can be printed when  $V_f$  is less than 40 vol%, while uncured HT/BT and HT/ST slurries can be printed when  $V_f$  is less than 20 vol%.

To analyze the influence of the inorganic ceramic fillers on the viscosity of the uncured slurries, the Maron–Pierce semiempirical model [24] is utilized:

$$\frac{\eta}{\eta_0} = \left(1 - \frac{V_f}{V_{\max}}\right)^{-2}, \quad (2)$$

where  $\eta$  (mPa·s) is the viscosity of the uncured slurry;  $\eta_0$  is the viscosity of the pure UV resin;  $V_f$  is the volume fraction of the fillers; and  $V_{\max}$  is the maximum volume fraction related to factors such as the microscopic morphologies of the fillers and interaction force between the particles.

When  $V_f$  is constant, for a greater  $V_{\max}$ , the lower is the viscosity of the uncured slurry. According to the fitting results in Figure 10(a), the model fits well when  $V_{\max}$  of Al<sub>2</sub>O<sub>3</sub>, SrTiO<sub>3</sub>, and BaTiO<sub>3</sub> are set to 63.29%, 32.95%, and 33.57%, respectively. It is seen that the  $V_{\max}$  of Al<sub>2</sub>O<sub>3</sub> is

TABLE 3: Flow activation energies of the pure resin and uncured composites with 20 vol% loading.

Sample	$E_\eta/\text{kJ}\cdot\text{Mol}^{-1}$	Sample	$E_\eta/\text{kJ}\cdot\text{Mol}^{-1}$
Pure resin	52.9	Pure resin	52.9
HT/AL-L-20	56.7	HT/AL-S-20	63.3
HT/ST-L-20	60.8	HT/ST-S-20	58.5
HT/BT-L-20	60.7	HT/BT-S-20	60.9

almost twice those of BaTiO<sub>3</sub> and SrTiO<sub>3</sub>, indicating that the fluidity of the uncured HT/AL slurry is significantly better than those of the other two slurries.

According to a previous work [24], the viscosity of the uncured slurry is mainly related to the morphology of the fillers. The energy loss of the uncured slurry during the flow process is relatively small with fillers having spherical shapes and smooth surfaces. Therefore, they will have better fluidities at the macro level, and  $V_{\max}$  will also have higher values. According to Figures 3, 5, and 6, Al<sub>2</sub>O<sub>3</sub> fillers have the above characteristics and can be dispersed well in the UV resin such that the uncured slurry has excellent fluidity regardless of the particle sizes of the Al<sub>2</sub>O<sub>3</sub> fillers. However, uncured HT/BT and HT/ST slurries have poor fluidities because the surfaces of the BT-L and ST-L fillers are rough and have irregular shapes with serious agglomerations in the UV resin.

In addition to the content and morphology of the fillers, the ambient temperature has a significant effect on the viscosity of the slurries. Taking the logarithm of the viscosity  $\eta$  of the pure resin and uncured slurries (20 vol%), the relationship between  $\ln \eta$  and  $1/T$  (unit: K) is as shown in Figure 10(b). It is seen that  $\ln \eta$  has an obvious linear

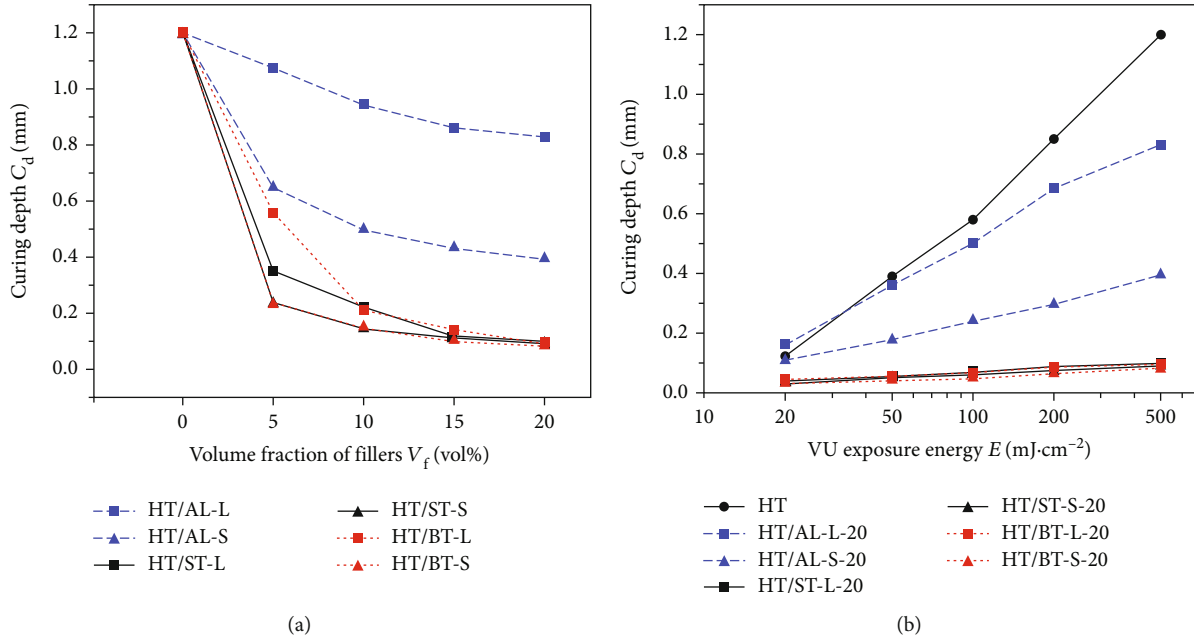


FIGURE 11: (a) UV curing depth of the pure resin and composites under different volume fractions of fillers and (b) UV curing depths of pure resin and composites under different UV exposure energies.

relationship with  $1/T$ ; as the temperature decreases, the viscosity also decreases, which conforms to the Arrhenius equation [25].

$$\eta = K e^{E_\eta / RT}, \quad (3)$$

where R is the gas constant ( $8.314 \text{ J}\cdot\text{mol}^{-1}\cdot\text{K}^{-1}$ ); K is the material constant; and  $E_\eta$  is the activation energy of viscous flow ( $\text{kJ}\cdot\text{mol}^{-1}$ ) that reflects the difficulty of flow of the uncured slurry and sensitivity of viscosity to temperature [26].

Using Equation (3) to fit the viscosity data of the uncured slurries at different temperatures, the  $E_\eta$  values of the pure resin and six uncured slurries are obtained. Table 3 shows that the  $E_\eta$  values of the six uncured slurries increase compared with that of the pure resin and that the viscosity is more sensitive to temperature changes. In the 3D-printing process, low viscosity can be reduced by increasing the temperature to improve the printing accuracy and success rate. However, too low viscosities will also cause settlement of the fillers, which needs to be further explored.

In the SLA process, the slurry with a certain thickness ( $\leq 200 \mu\text{m}$ ) is cured layerwise under UV exposure. If the curing depth of the slurry is too thin, it will cause printing failure such as peeling of the bottom plate and peeling between the layers. Figure 11(a) shows the relationships between the curing depths of the composites and volume fractions of the fillers under UV exposure ( $500 \text{ mJ}/\text{cm}^2$ ). Figure 11(b) depicts the curing depths of the pure resin and six composites with different fillers (20 vol%) under different exposure energies. It is seen that the introduction of inorganic fillers reduces the curing depths of the composites. The larger the particle sizes of the fillers, the thicker are the curing depths

of the composites. For instance, under UV exposure ( $500 \text{ mJ}/\text{cm}^2$ ), the curing depth of the HT/AL-L composites (20 vol%) is 0.83 mm, while that of the HT/AL-S composites is only 0.395 mm for the same volume fraction.

It is generally believed that a decrease in the curing depths of the composites for filling with inorganic fillers is related to the scattering of light by the filler particles [12]. According to the Beer–Lambert law, the curing depth of the composites satisfies Equation (4): [27]

$$C_d = D_p \ln (E/E_c), \quad (4)$$

where  $C_d$  is the curing depth,  $E$  is the UV exposure energy;  $E_c$  is the critical UV exposure energy that reflects the energy required when the UV resin starts curing, and its value mainly depends on the UV resin formulation and oxygen content; and  $D_p$  is the transmission depth coefficient and is closely related to the refractive index, morphology, and volume fraction of the fillers, the specific relationship is shown in formula (5) [27].

$$D_p \propto \frac{2 D_{50} \lambda n_0}{3 \phi_f \Delta n^2}, \quad (5)$$

where  $D_{50}$  is the average particle size of the fillers,  $\lambda$  is the wavelength of the incident UV radiation;  $\phi_f$  is the volume fraction of the fillers;  $n_0$  is the refractive index of the UV resin matrix; and  $\Delta n$  is the difference between the refractive index of the fillers and UV resin matrix, i.e.,  $\Delta n = n_f - n_0$ .

For particle-filled composites, when the wavelengths of the UV radiation and resin type are constant, the composites with small-sized filler particles, high refractive index, and high filling content have a stronger scattering effects with

TABLE 4: Physical properties of the fillers related to UV curing.

Filler	Particle size $D_{50}/\mu\text{m}$	Refractive index $n_f$	$\Delta n$
HT	/	1.50	/
$\text{Al}_2\text{O}_3\text{-S}$	2.17		
$\text{Al}_2\text{O}_3\text{-L}$	31.07	1.76	0.26
$\text{SrTiO}_3\text{-S}$	3.71		
$\text{SrTiO}_3\text{-L}$	32.58	2.39	0.89
$\text{BaTiO}_3\text{-S}$	3.27		
$\text{BaTiO}_3\text{-L}$	32.09	2.40	0.90

UV radiation such that  $D_p$  is smaller and the curing depth is thinner [28], which is consistent with Figure 11. On the other hand, Table 4 depicts that  $\text{BaTiO}_3$  and  $\text{SrTiO}_3$  fillers have close refractive indices that are significantly higher than those of the  $\text{Al}_2\text{O}_3$  fillers and UV resin matrix ( $n = 1.50$ ). Therefore, the curing depths of the HT/BT and HT/ST composites are lower, which is consistent with the experimental results.

In summary, fillers with spherical shape, smooth surface, and good dispersion in the matrix need to be selected, as well as the printing temperature can be increased appropriately without causing significant sedimentation, which can obtain low-viscosity slurry suitable for SLA technology. In addition, in order to achieve such composites' 3D printing, the light transmittance of the composites can be improved by increasing the particle size of the fillers appropriately. Moreover, the parameters of 3D printing need to be adjusted to increase the UV exposure energy. When the UV exposure energy is more than  $500 \text{ mJ/cm}^2$ , the composites with  $\text{BaTiO}_3$  fillers (20 vol%) can reach curing depth of 0.1 mm (Figure 10(b)), which is feasible for 3D printing.

## 4. Conclusion

In this contribution, we obtained composite slurry with high permittivity by adding  $\text{BaTiO}_3$  to the UV resin and proved the addition of  $\text{Al}_2\text{O}_3$  has little effect on HT/AL composites' dielectric properties, which means that  $\text{Al}_2\text{O}_3$  is the ideal filler in the double-filler system. Meanwhile, spherical  $\text{Al}_2\text{O}_3$  with smooth surfaces reduced HT/AL slurry's viscosity significantly and the curing depths can be enhanced by increasing the particle sizes of the fillers. The underlying mechanisms of aforementioned phenomena were studied in depth and determined as follows: (i) The increase in the permittivity of HT/BT composites is attributed to the filler's high intrinsic permittivity and interface polarization. (ii) The spherical fillers with smooth surfaces have better dispersibility in the resin matrix and less energy loss during flow process; thus, HT/AL composites exhibit better fluidity. (iii) Large particle size fillers can reduce the scattering of UV radiation, leading to the improvement of curing depths of large particle size filler composite system.

We believe that the relative permittivities of the composites can be adjusted over a wide range, their viscosities can be reduced, and the curing depths can be enhanced using spherical  $\text{BaTiO}_3$  fillers with large-sized particles having

smooth surfaces and high relative permittivities. This composite system is expected to be used in the preparation of  $\epsilon$ -FGM by SLA. However, how to solve the settlement of the fillers when the viscosities are too low and maintain the stability of the viscosity of the slurry along the gradient direction to reduce the difficulty of printing need to be considered in a future study.

## Data Availability

The data that support the findings of this study are available from the corresponding author upon reasonable request.

## Conflicts of Interest

The authors declare that they have no conflicts of interest.

## Acknowledgments

This work was financially supported by the National Natural Science Foundation of China (No. U1766218).

## References

- [1] S. J. Cheng, "Progress in advanced electrical materials," *Proceedings of the CSEE*, vol. 37, no. 15, pp. 4273–4285, 2017.
- [2] Z. Yan and D. H. Zhu, *High Voltage Insulation Technology*, China Electric Power Press, Beijing, 2nd ed edition, 2007.
- [3] Z. Stih, "High voltage insulating system design by application of electrode and insulator contour optimization," *IEEE Transactions on Electrical Insulation*, vol. EI-21, no. 4, pp. 579–584, 1986.
- [4] Z. B. Wang, W. G. Gu, Z. Q. Rao, H. Lv, X. W. Li, and J. Wu, "Research on ultra-high frequency receiving characteristic of GIS basin-type insulator grading ring," *Guangdong Electric Power*, vol. 27, no. 12, pp. 96–101, 2014.
- [5] X. C. Sun, Z. R. Peng, Z. P. Dang, J. L. Ding, and T. T. Wang, "Study on electrical stress grading of composite insulators for UHV transmission lines," *High Voltage Apparatus*, vol. 44, no. 6, pp. 527–530, 2008.
- [6] S. Liu, P. Jiang, C. G. Peng, and X. J. Shao, "Analysis on breakdown failure in basin-type insulator of 1100 kV GIS," *Zhejiang Electric Power*, vol. 35, no. 10, pp. 36–39, 2016.
- [7] M. Koizumi, "FGM activities in Japan," *Composites Part B-Engineering*, vol. 28, no. 1-2, pp. 1–4, 1997.
- [8] S. Suresh and A. Mortensen, *Fundamentals of Functionally Gradient Materials*, National Defend Industry Press, Beijing, 2000.
- [9] K. Kato, M. Kurimoto, H. Shumiya, H. Adachi, H. Okubo, and S. Sakuma, "Application of functionally graded material for solid insulator in gaseous insulation system," *IEEE Transactions on Dielectrics and Electrical Insulation*, vol. 13, no. 2, pp. 362–372, 2006.
- [10] T. Nardi, N. Mora, F. Rachidi, and Y. Leterrier, "Graded-permittivity polymer nanocomposites as superior dielectrics," *Composites Science and Technology*, vol. 129, no. Jun. 6, pp. 1–9, 2016.
- [11] G. J. Zhang, W. D. Li, Z. Liu et al., "Research progress on dielectric functionally gradient materials for electrical insulation," *Proceedings of the CSEE*, vol. 37, no. 14, pp. 4232–4245, 2017.

- [12] M. L. Griffith and J. W. Halloran, "Freeform fabrication of ceramics via stereolithography," *Journal of the American Ceramic Society*, vol. 79, no. 10, pp. 2601–2608, 1996.
- [13] Y. Q. Yang, L. Xu, and H. Y. Jin, "Preparation of spherical silica powder by oxygen-acetylene flame method," *Journal of Wuhan University of Technology*, vol. 33, no. 9, pp. 37–40, 2011.
- [14] R. Mondal, A. Das, D. Sen, D. K. Satapathy, and M. G. Basavaraj, "Spray drying of colloidal dispersions containing ellipsoids," *Journal of Colloid and Interface Science*, vol. 551, pp. 242–250, 2019.
- [15] X. W. Chen, J. X. Li, and H. A. Liu, "Research progress of rapid prototyping and photocurable resin," *Laser Journal*, vol. 32, no. 3, pp. 1–3, 2011.
- [16] Z. M. Dang, J. K. Yuan, J. W. Zha, T. Zhou, S. T. Li, and G. H. Hu, "Fundamentals, processes and applications of high-permittivity polymer-matrix composites," *Progress in Materials Science*, vol. 57, no. 4, pp. 660–723, 2012.
- [17] H. Wen, X. H. Wang, R. Z. Chen, L. T. Li, and Z. L. Gui, "Dielectric properties of barium titanate-based X7R ceramics mixed with different grain sizes," *Rare Metal Materials and Engineering*, vol. 34, no. 2, pp. 923–926, 2005.
- [18] S. Singha and M. J. Thomas, "Dielectric properties of epoxy nanocomposites," *IEEE Transactions on Dielectrics and Electrical Insulation*, vol. 15, no. 1, pp. 12–23, 2008.
- [19] M. Kurimoto, H. Ozaki, Y. Yamashita, T. Funabashi, T. Kato, and Y. Suizuiki, "Dielectric properties and 3D printing of UV-cured acrylic composite with alumina microfiller," *IEEE Transactions on Dielectrics and Electrical Insulation*, vol. 23, no. 5, pp. 2985–2992, 2016.
- [20] L. Lan, J. Wu, Z. Ji, and D. Yu, "Breakdown properties of nano-SiO<sub>2</sub>/LDPE composites," *Proceedings of the CSEE*, vol. 32, no. 13, pp. 138–143, 2012.
- [21] D. R. Xie, D. M. Min, Y. Huang, W. B. Kang, S. Z. Ren, and S. T. Li, "Nano-doping effects on dielectric breakdown and corona-resistance properties of polymeric nanocomposites," *Proceedings of the CSEE*, vol. 38, no. 19, pp. 5909–5918, 2018.
- [22] W. D. Li, Z. Liu, X. Y. You, X. R. Li, and G. J. Zhang, "Permittivity distribution optimization for multi-layer dielectric FGM insulator," *Journal of Xi'an Jiaotong University*, vol. 50, no. 10, pp. 19–26, 2016.
- [23] T. Kataoka, T. Kitano, M. Sasahara, and K. Nishijima, "Viscosity of particle filled polymer melts," *Rheologica Acta*, vol. 17, no. 2, pp. 149–155, 1978.
- [24] S. Muller, E. W. Llewellyn, and H. M. Mader, "The rheology of suspensions of solid particles," *Proceedings of the Royal Society a-Mathematical Physical and Engineering Sciences*, vol. 466, no. 2116, pp. 1201–1228, 2010.
- [25] L. E. Nielsen, Q. R. Fan, and J. Q. Song, *Polymer Rheology*, Science Press, Beijing, 1983.
- [26] Y. Teng, S. Wang, J. Wang, and S. X. Li, "Effect of montmorillonite content on dynamic rheological behavior of polyethylene/montmorillonite nanocomposite," *Journal of Functional Materials*, vol. 46, no. 11, pp. 11089–11093, 2015.
- [27] N. Travitzky, A. Bonet, B. Dermeik et al., "Additive manufacturing of ceramic-based materials," *Advanced Engineering Materials*, vol. 16, no. 6, pp. 729–754, 2014.
- [28] Y. Yang, Z. Y. Chen, X. Song et al., "Three dimensional printing of high dielectric capacitor using projection based stereolithography method," *Nano Energy*, vol. 22, pp. 414–421, 2016.